

原子层沉积与聚焦离子束切片法制备 X 射线波带片

谭民生^{1,3}, 明帅强¹, 吴雨菲^{1,3}, 卢维尔^{1,3*}, 李艳丽^{2**}, 孔祥东^{2,3***}, 刘海岗⁴, 夏洋^{1,3}, 韩立^{2,3}¹中国科学院微电子研究所, 北京 100029;²中国科学院电工研究所, 北京 100190;³中国科学院大学, 北京 100049;⁴中国科学院上海高等研究院上海同步辐射光源, 上海 201800

摘要 针对 X 射线波带片对大高宽比的应用需求, 采用原子层沉积法在光滑的金属丝表面生长膜厚可高精度控制的多层膜环带结构, 再利用聚焦离子束切片技术获得大高宽比的多层膜 X 射线波带片。采用复振幅叠加法设计了以 Al₂O₃/HfO₂ 分别为明环和暗环材料的 X 射线波带片, 实验上利用原子层沉积在直径为 72 μm 的金丝表面交替沉积了 10.11 μm 的 Al₂O₃/HfO₂ 多层膜, 环带数为 356, 总直径为 92.22 μm, 最外环宽度为 25 nm。通过聚焦离子束切割得到高为 1.08 μm、高宽比达 43:1 的 X 射线多层膜菲涅耳波带片。该波带片应用于上海光源(BL08U1A)软 X 射线成像线站时, 在 1.2 keV X 射线下实现聚焦成像功能, 展现出利用该技术制备多层膜 X 射线波带片的潜力。

关键词 X 射线菲涅耳波带片; 原子层沉积; 聚焦离子束; 大高宽比; 多层膜

中图分类号 O436

文献标志码 A

DOI: 10.3788/AOS222052

1 引言

X 射线具有能量高和穿透性强的特点^[1], 利用物质对 X 射线的穿透性差异可以对其内部结构进行探测。新一代同步辐射大科学装置提供了高亮度、高准直、高能量分辨、宽波段连续可调的优质 X 射线, 在金属探伤、细胞成像、材料检测等领域应用广泛^[2-4]。用于 X 射线的光学元件主要包括 X 射线毛细管、K-B 镜、多层膜劳厄透镜、多层膜反射镜、复合折射透镜、X 射线波带片等^[5-9]。其中, X 射线波带片被认为是最有潜力提高 X 射线显微成像质量的元件之一^[10]。X 射线波带片是由两种不同的材料按照线密度由内向外逐渐增大的规则交替排列组合而成的同心圆环^[11], 利用圆环带对 X 射线的衍射原理实现聚焦成像^[10-12]。评价 X 射线波带片性能的技术指标主要有两个: 成像空间分辨率和衍射效率。根据瑞利判据^[13], 在理想环带情况下, 波带片的成像分辨率 $\delta = 1.22\Delta r_N$ 。其中, Δr_N 为最外环宽度, 即最外环宽度越小, 分辨率越高。衍射效率与 X 射线的能量、材料在入射 X 射线下的折射率以及波带片的高度密切相关。在 X 射线波段, 由于 X 射线的穿透性强, 要实现波带片的高分辨成像和高衍射效率, 需要在减小波带片最外环宽度的同时提高波带片高

度, 使得相邻两个波带有 π 的相位差达到相干衍射^[14], 即波带片的高宽比(高度/最外环宽度)大, 而大高宽比波带片的制备又一直是微纳加工领域的一大难题。

目前, X 射线波带片的类型主要分为两种: 镂空型波带片和多层膜型波带片。镂空型波带片利用氮化硅或者碳化硅薄膜作为机械支撑, 环带结构在支撑膜上, 主要制备方法包括激光全息曝光法^[15-16]和电子束光刻法(EBL)^[17-21]等。其中, EBL 作为光刻工艺中精度最高的技术, 成为 X 射线显微成像系统所用波带片的主要制备方法^[17-21], 主要的工艺路线是在预先沉积好金属种子层的基底上采用 EBL 曝光获得环带图形, 再利用金属电镀的方法来改善波带片厚度^[17-18], 该技术制备的金属波带片最外环宽度可小到 20~30 nm, 但高度被限制在 750~900 nm 以下, 高宽比约为 35^[17-21]。多层膜型波带片将镂空部分用另一种材料替代, 在中心细丝表面交替沉积两种薄膜材料, 结构稳定性好, 沉积完成后利用切片法可获得任意大高度, 这对于制备大高宽比波带片具有独特的优势。已报道的多层膜制备方法包括磁控溅射(MS)法^[22-25]、脉冲激光沉积(PLD)^[26]和原子层沉积(ALD)法^[10-12, 27-30]。Takano 等^[24]利用 MS 法在玻璃光纤表面交替沉积了 178 层 MoSi₂/Si 多层膜, 最外环宽度为 25.2 nm, 切割得到

收稿日期: 2022-11-25; 修回日期: 2023-02-15; 录用日期: 2023-02-21; 网络首发日期: 2023-03-09

基金项目: 中国科学院团队项目(GJJSTD20200003)、自然科学基金项目(12104454)、中国科学院电工研究所基金项目(E1554404)

通信作者: *luweier@ime.ac.cn; **liyanli@mail.iee.ac.cn; ***slkongxd@mail.iee.ac.cn

67 μm 厚的超大高宽比波带片。Eberl 等^[26]利用 PLD 法以玻璃光纤为基底制备了 $\text{Ta}_2\text{O}_5/\text{ZrO}_2$ 多层膜波带片,最外环宽度为 10 nm,高宽比达到 800。MS 和 PLD 属于物理气相沉积(PVD)法,在圆柱基底表面沉积薄膜时,需要旋转基底进行镀膜以提高薄膜的均匀性,薄膜的保形性很难控制。ALD 技术因其自限制气相化学吸附的特点,膜厚精度为原子级别,且所沉积的薄膜具有很好的均匀性和保形性。Sanli 等^[27]曾采用 ALD 技术在玻璃光纤表面制备出总直径为 39.4 μm 、最外环宽度为 25 nm、高宽比为 500:1 的 X 射线波带片,波带片的总直径小、有效聚光面积小。

本文根据上海光源同步辐射大科学装置实验线站(BL08U1A)的光路需求,设计并制备了大尺寸的 X 射线波带片。采用复振幅叠加法^[31]设计了环带数为 356、总膜厚达 10 μm 的 $\text{Al}_2\text{O}_3/\text{HfO}_2$ 多层膜结构 X 射线波带片,利用 ALD 技术在光滑的金丝基底表面交替沉积两种薄膜。由于薄膜的沉积时间长,通过陪片监测薄膜的厚度与生长速率,实现了原子级精度的薄膜沉积,充分发挥了 ALD 膜厚精确可控的优势。利用聚焦离子束(FIB)切割、抛光,获得了最外环宽度为 25 nm、高宽比达 43:1 的 X 射线波带片,并在同步辐射成像线站上实现了聚焦成像。

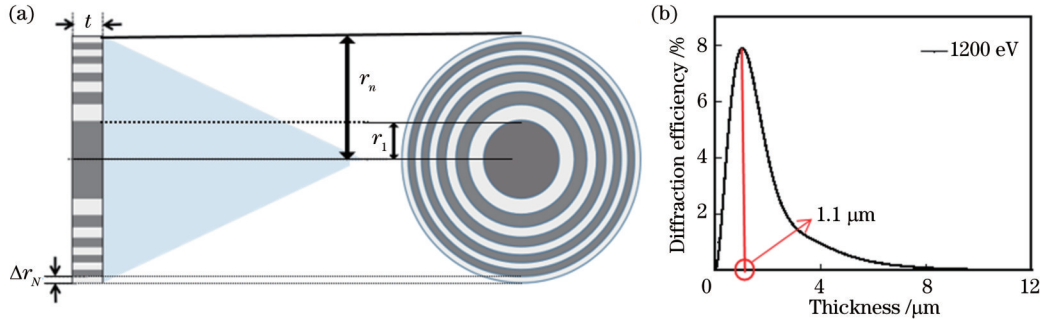


图 1 X 射线波带片的结构设计。(a)波带片结构示意图;(b) X 射线能量为 1.2 keV 时 $\text{Al}_2\text{O}_3/\text{HfO}_2$ 多层膜波带片衍射效率随高度的变化曲线

Fig. 1 Structural design of X-ray zone plate. (a) Structure diagram of zone plate; (b) variation of diffraction efficiency of $\text{Al}_2\text{O}_3/\text{HfO}_2$ zone plate with thickness at 1.2 keV

表 1 X 射线波带片的结构设计参数

Table 1 Structural design parameters of X-ray zone plate

X-ray energy E/keV	Diameter of zone plate $D/\mu\text{m}$	Diameter of central substrate $d/\mu\text{m}$	Outermost zone width $\Delta r_N/\text{nm}$	Thickness of zone plate $t/\mu\text{m}$	Focal length f/mm	Number of zones n
1.2	92	72	25	1.1	2.23	356

2.2 工艺制备

X 射线多层膜波带片的制备工艺路线如图 2 所示,首先利用 ALD 在直径为 72 μm 的金丝表面交替沉积 356 环 10 μm 厚的 $\text{Al}_2\text{O}_3/\text{HfO}_2$ 多层膜,每一层的膜厚严格根据预先设计好的波带片环带宽度,然后采用 FIB 切割、转移并抛光得到所设计高度 1.1 μm 的波带片。

2 波带片的制备

2.1 结构设计

X 射线菲涅耳波带片由一组同心圆环组成,如图 1(a) 所示,其环带宽度 Δr_n (即多层膜的膜层厚度)由内向外径向递减,且 $\Delta r_n = \sqrt{n\lambda f} - \sqrt{(n-1)\lambda f}$ 。其中, n 为波带片的环带数, λ 为 X 射线的波长, f 为焦距。在 X 射线波段,物质的折射率 $n_i = 1 - \alpha - i\beta$, 其中, α 为相位项, β 为材料的吸收系数。当 X 射线能量为 1.2 keV 时, Al_2O_3 和 HfO_2 对 X 射线的吸收系数和相位差异较大,且它们的熔点高、化学性质稳定,有着较大的 ALD 共同温度生长区间,因此采用 $\text{Al}_2\text{O}_3/\text{HfO}_2$ 作为多层膜材料。波带片的一级衍射效率 E_{ff} 根据复振幅叠加法^[31] 计算: $E_{\text{ff}} = \frac{1}{\pi^2} \{ \exp(-2k\beta_1 t) + \exp(-2k\beta_2 t) - 2\exp[-2k(\beta_1 + \beta_2)] \cos[kt(\alpha_1 - \alpha_2)] \}$ 。其中, t 为波带片的高度, $k = 2\pi/\lambda$ 。 $\text{Al}_2\text{O}_3/\text{HfO}_2$ 多层膜波带片的衍射效率随高度变化的曲线如图 1(b) 所示。可以看出,波带片的高度为 1.1 μm 时,衍射效率最大。因此,结合 BL08U1A 的光路特点,所设计的 $\text{Al}_2\text{O}_3/\text{HfO}_2$ 多层膜波带片结构如表 1 所示。

在沉积多层膜前,用超声清洗金丝并用高纯氮气吹干。金丝的长度为 5~10 mm,表面粗糙度小于 0.3 nm,将金丝的一段通过高温胶带固定在硅片上,另一端悬空,用于多层膜生长,一次可同时在多根金丝表面沉积多层膜,因此可实现波带片的批量化制备。由于多层膜的厚度高达 10 μm ,沉积的时间相对较长,为校正薄膜厚度的偏移,沉积过程中将硅片作为膜厚

检测的陪片,通过硅片上薄膜厚度的测量值修正薄膜厚度。

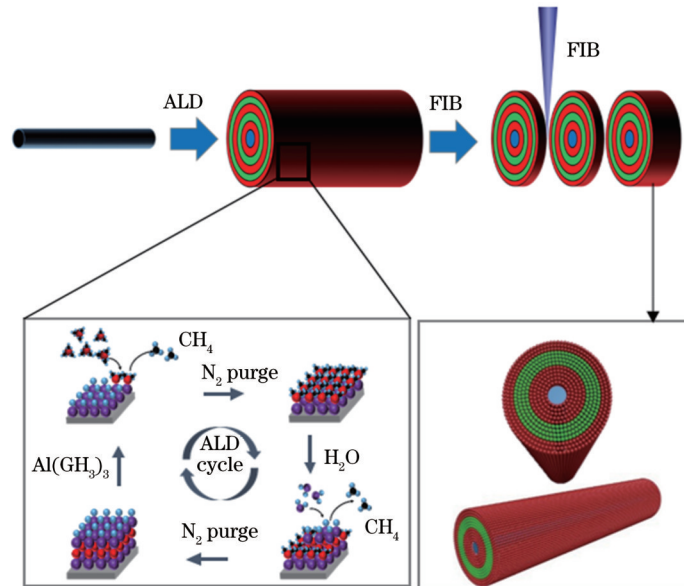


图 2 X 射线多层膜波带片制备工艺路线图

Fig. 2 Process roadmap for preparing X-ray multilayer zone plates

制备多层膜所使用的 ALD 设备为自研的双腔快速原子层沉积系统,该设备引入双腔真空气流场技术,利用内外双真空腔的强气体流速缩短反应周期,极大地提高薄膜的生长效率,从而缩短多层膜的沉积时间。沉积的工艺参数如下:管路温度 120 °C,衬底温度 150 °C,工艺真空 0.2 Torr (1 Torr=133.322 Pa)。Al₂O₃ 薄膜制备工艺条件为腔室内脉冲通入三甲基铝 (TMA) 0.02 s, N₂ 吹扫 10 s, 腔室内通入去离子水 0.015 s, N₂ 吹扫 10 s。HfO₂ 薄膜制备的工艺条件为腔室内脉冲通入四(二甲胺基) 钪 (TDMAH) (加热至 75 °C) 0.08 s, N₂ 吹扫 15 s, 腔室内通入去离子水 0.015 s, N₂ 吹扫 10 s。薄膜的厚度通过椭偏仪 (Horiba Uvisel 2) 和扫描电子显微镜 (SEM, Zeiss Sigma) 测量。

多层膜 ALD 沉积工艺结束后,采用电子束蒸发法 (ZZSX-500) 在多层膜细丝表面制备 ~300 nm 铬 (Cr) 保护膜,防止后续 FIB 切割对多层膜环带的损伤。然后利用 FIB (Thermo Fisher Scios 2) 大束流镱离子进行切割,束流为 65 nA,为了后续操作方便,利用双束系统中的微机械臂将切割完成的波带片转移到透射电子显微镜 (TEM) 用的铜载网上,接着逐渐减小镱离子束流,对波带片的两个表面进行抛光,最小束流为 5 nA,最后得到特定高度的 X 射线波带片。

3 结果与分析

为了验证 ALD 生长薄膜的均匀性,预先在硅衬底上沉积周期数分别为 300、500 和 600 的 Al₂O₃ 和 HfO₂ 薄膜,使用椭偏仪在样品中心横、纵两个方向取 9 个采样点,测试所得的薄膜厚度如图 3 所示,数字单位为

Å (1 Å=1×10⁻¹⁰ m)。

根据公式 $(d_{\max} - d_{\min})/2d_{\text{mean}}$ 可得到 Al₂O₃ 薄膜的非均匀性分别为 ±0.31%、±0.13% 和 ±0.11%, HfO₂ 薄膜的非均匀性为 ±0.27%、±0.08% 和 ±0.07%。其中, d_{\max} 和 d_{\min} 分别为采样点中薄膜厚度的最大值和最小值、 d_{mean} 为采样点薄膜厚度的平均值。膜厚小于 ±1% 的非均匀性满足多层膜波带片沉积需求。进而可计算得到 Al₂O₃ 和 HfO₂ 薄膜的平均生长速率,分别为 0.96 Å/cycle 和 1.20 Å/cycle,用于多层膜初始沉积工艺。

鉴于波带片膜厚高达 10 μm,而每层环带的控制精度要在原子精度,考虑以单一初始速率进行沉积的技术方案可能存在膜厚控制误差。多层膜的 ALD 生长速率会受到腔室温度、真空度以及气流等的影响,为了提高多层膜厚度的控制精度,在波带片沉积腔室的不同位置放置小尺寸硅片基底作为陪片,通过监测陪片上多层膜的生长情况及时校正薄膜生长速率。首先以初始生长速率进行前 40 环的多层膜沉积,通过 SEM 测量陪片多层膜的膜厚,计算出实际膜厚的平均值与标准差,得到平均生长速率,然后以校正过的生长速率进行接下来 40 环薄膜的生长,以此方式迭代,直至沉积完所有的环带。

图 4(a) 为陪片部分环带的 SEM 图像,按照环带数每沉积 40 环进行一次取样测试,利用 SEM 测试该 40 层多层膜的膜厚数据,每层薄膜测试 5 个膜厚数据,根据 $\bar{t} = (t_1 + t_2 + t_3 + \dots + t_n)/n$ 计算平均值和 $\sigma = \sqrt{(t_1 - \bar{t})^2 + (t_2 - \bar{t})^2 + (t_3 - \bar{t})^2 + \dots + (t_n - \bar{t})^2}/n$ 计算标准差,按照此方法对实验中所有多层膜进行测试分析。表 2 为其中 9 个环带的膜厚测试与计算详细数

Al ₂ O ₃	318.3	300 cycles	318.6	317.5	487.1	486.6	486.5	486.2	487.2	517.1	517.9	517.9	517.9	518.3
	317.6													
	319.1													
	318.0													
HfO ₂	367.0	300 cycles	368.8	368.1	599.2	598.2	598.7	598.3	599.1	693.8	694.2	693.7	693.8	693.5
	367.5													
	367.8													
	368.5													

图 3 Al₂O₃和HfO₂薄膜厚度的椭偏仪测试结果

Fig. 3 Ellipsometer test results of Al₂O₃ and HfO₂ film thickness

据,实际膜厚与理论膜厚的对比曲线及实际膜厚误差棒信息图如图 4(b)所示。可以看出,经过及时的生长

速率校正后,多层膜的实际膜厚与理论膜厚曲线一致性较好,平均膜厚误差均小于 2 nm。

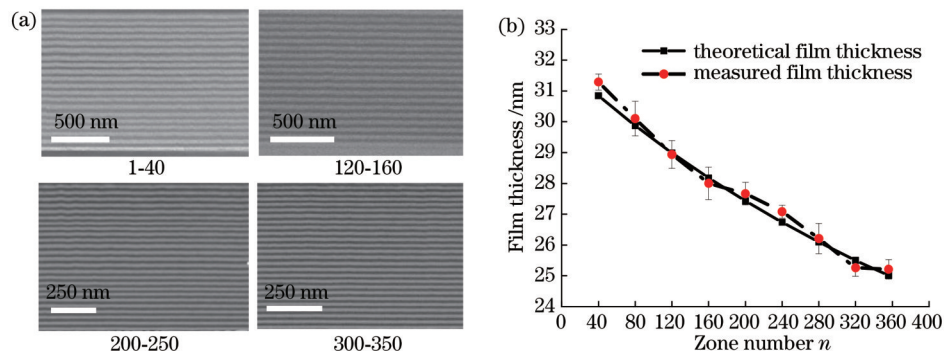


图 4 速率校正结果。(a) 陪片部分环带的 SEM 图;(b) 理论膜厚与实际膜厚的对比曲线

Fig. 4 Rate correction result diagram. (a) SEM images of multilayer films on Si slices; (b) the comparison curve between theoretical and measured film thickness

表 2 部分多层膜膜厚测试数据

Table 2 Test data of typical multilayer films

Zone number	Measured t_1 / nm	Measured t_2 / nm	Measured t_3 / nm	Measured t_4 / nm	Measured t_5 / nm	Average t / nm	Standard error / nm	Theoretical t / nm
40	31.20	31.02	31.66	31.12	31.46	31.29	0.26	30.84
80	30.55	29.35	30.41	29.65	30.55	30.10	0.56	29.87
120	29.62	28.43	28.78	29.10	28.76	28.94	0.45	28.98
160	28.68	27.22	28.10	27.88	28.12	28.00	0.53	28.17
200	27.90	27.22	27.88	28.02	27.32	27.67	0.37	27.43
240	27.12	26.94	27.25	26.80	27.30	27.10	0.21	26.74
280	26.98	25.67	25.98	26.32	26.10	26.21	0.49	26.10
320	25.62	24.96	25.20	25.45	25.07	25.26	0.27	25.50
360	25.56	24.86	25.23	24.92	25.48	25.21	0.32	25.02

完成 ALD 多层膜沉积及 Cr 保护层后,利用 FIB 进行波带片的切割和抛光。由于波带片的尺寸很大,切割、转移的过程不同于一般的小样品,切割过程要注意确认两面是否完全切断,考虑溅射损伤的影响,预留的波带片高度要足够。提取过程中,微机械臂粘接样

品时,沉积 Pt 的时间要适当延长;固定在铜载网的操作过程中,为了保证波带片和载网稳定粘接,沉积 Pt 时采用双面沉积,即完成一面 Pt 沉积后翻转波带片,在另一面进行也进行 Pt 沉积。通过研究不同 FIB 工艺参数对切割速度、溅射损伤、转移效率、抛光面积和

抛光深度等的影响后,切割采用的参数设置如下:加速电压为 30 kV,切割束流为 65 nA,提取时沉积 Pt 的束流为 50 pA,时间约为 10 min,固定到铜载网时沉积 Pt 的束流为 3 nA,双面沉积时间约为 40 min,抛光束流为 5~15 nA。图 5(a)~(c)分别为切割、提取、转移固定波带片的过程图,图 5(d)~(f)分别是波带片俯视、截面和局部放大的 SEM 图。可以看出,波带片的总直径为 92.22 μm 、高度为 1.08 μm 、多层膜的总厚度为 10.11 μm ,且多层膜膜厚精度高、界面清晰、保形性

好,体现了原子层沉积技术的优势。然而,由于保形性沉积的多层膜厚度较大,在多层膜沉积、后续切割、转移和固定过程中因薄膜应力释放出现了结构缺陷,如图 5(e)方框和箭头所示。图 6 为缺陷位点局部放大 SEM 图。可以看出,缺陷主要包括多层膜断裂、多层膜与基底之间的界面裂痕以及外层多层膜的环带分裂,这些结构缺陷容易引起多层膜环带位置和环带厚度误差,对波带片的聚焦成像性能产生影响。可见应力的控制对于总厚度较大的多层膜沉积至关重要。

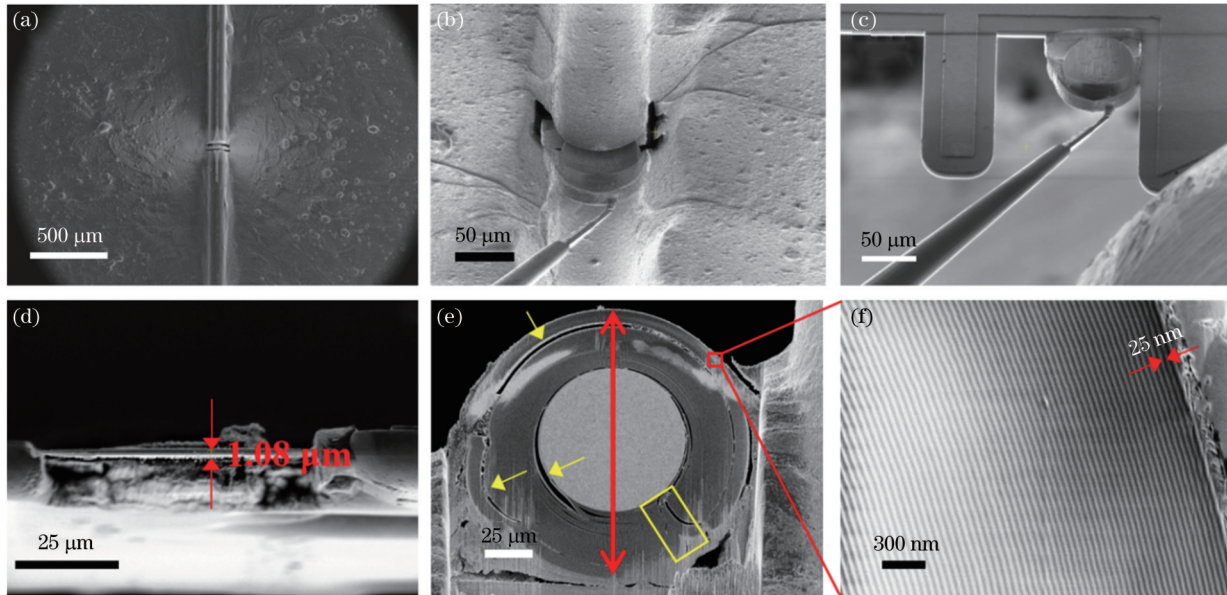


图 5 多层膜波带片 FIB 切片过程和制备完成 SEM 图。(a)切割;(b)提取;(c)转移固定;(d)俯视图;(e)截面图;(f)部分放大图
Fig. 5 SEM images of FIB slicing process and prepared zone plate. (a) Cutting; (b) extraction; (c) transfer and fixation; (d) top view; (e) sectional view; (f) partial enlarged view

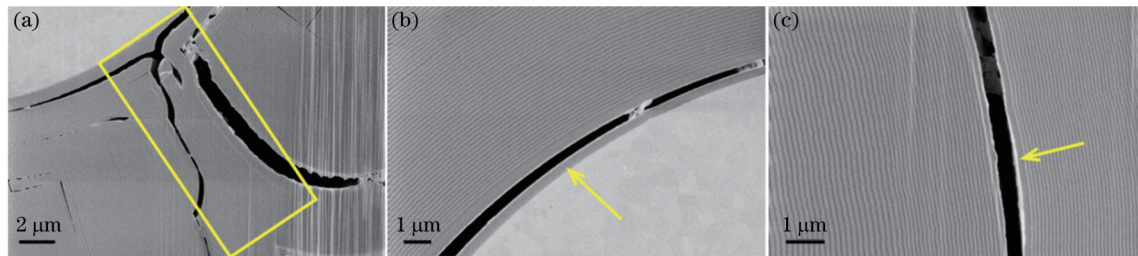


图 6 多层膜波带片缺陷位点局部放大 SEM 图。(a)多层膜断裂;(b)多层膜与基底之间出现界面裂痕;(c)外层多层膜环带分裂
Fig. 6 Partial enlarged SEM images of defects in multilayer zone plates. (a) Crack through the whole zone part; (b) interfacial crack between multilayers and substrate; (c) crack in the outer zones

将制备的波带片在上海光源软 X 射线谱学显微线站^[32]进行测试,结果如图 7 所示。线站能量范围为 0.25~2 keV,波荡器产生的 X 射线经过椭圆柱面镜聚焦、光栅单色器单色化和出射狭缝选择等操作后满足了实验站需求的高能量分辨率的高相干光的条件。考虑到波带片的透过率特性,入射光能量设定为 1.2 keV。采用扫描透射 X 射线显微成像方法进行测试,具体光路如图 7(a)所示。待测量波带片装在三维运动的滑台支架上[图 7(d)],波带片中心金丝直径为

72 μm ,因此采用直径为 50 μm 的级选光阑(OSA)去除波带片的直透光和高级衍射光。样品采用镀金星形标准靶,SEM 照片如图 7(b)、(c)所示,镀金星形标准靶的条幅宽度由外到内依次减小,分别为 800、400、200、100、50 nm,将星形标准靶样品放置于波带片一级聚焦的焦点处,采用光电倍增管(PMT)探测器采集透过标准靶的光信号。首先对整个样品进行扫描获取星形结构位置,如图 7(e)所示,扫描成像时移动步长设置为 200 nm,进而对星形靶中心区域进行精细扫描

成像,扫描步长设置为 20 nm,如图 7(f)所示。由图 7(f)可以看出星形靶的整体轮廓,从图中箭头标注可知成像分辨率约为 800 nm。分辨率不高的原因可能有以下几个方面:1)波带片多层膜的整体膜厚还较小,引起聚光的面积不足;2)多层膜应力释放过程引起多层膜开裂,如图 6 所示,进而出现环带误差,导致焦点处

的圆形光斑出现畸形,且焦点处实际光斑尺寸远大于设计值,从而导致标准靶的条幅模糊不清。因此,下一步将优化多层膜膜系组合,采用复合叠层结构正反应力抵消等工艺降低应力或消除应力带来的负面影响,并进一步提高多层膜厚度增加有效聚光面积,从而提高成像分辨率。

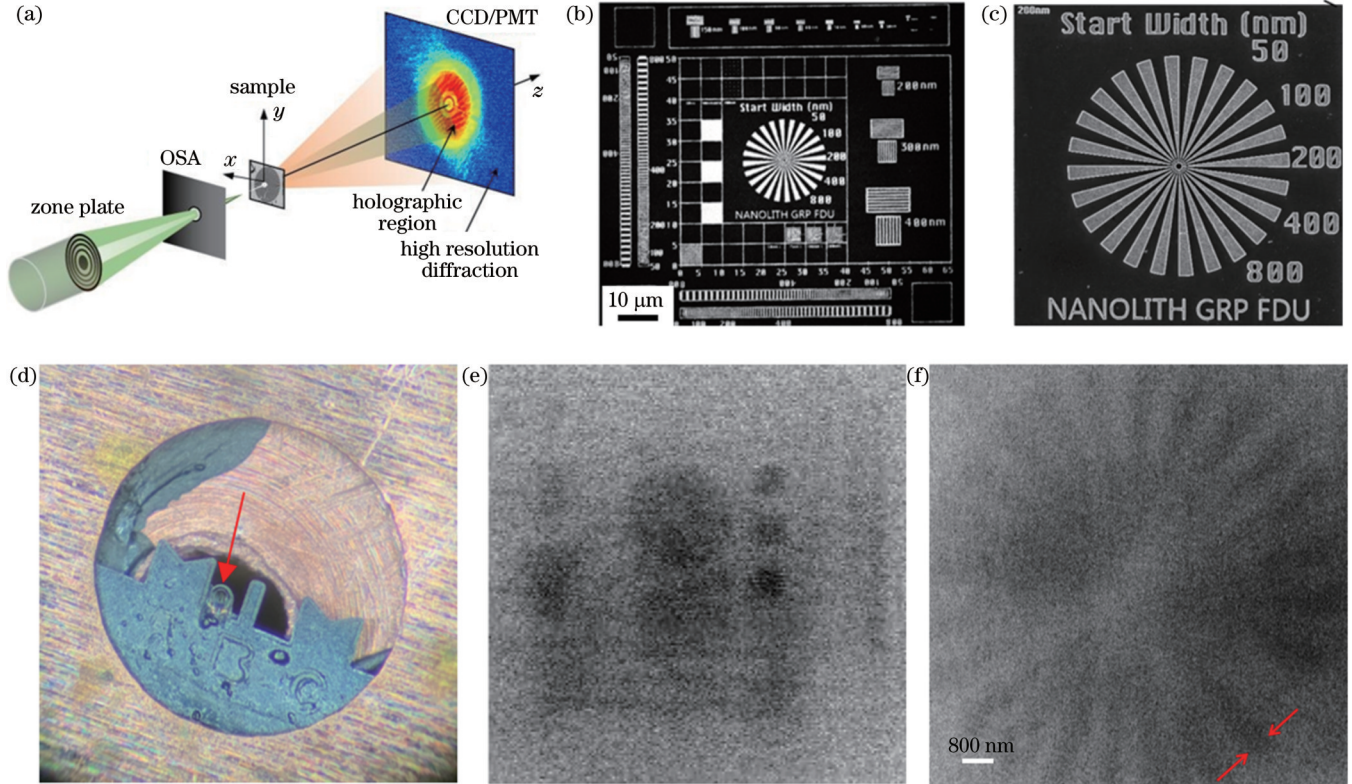


图 7 X 射线波带片的成像测试。(a)测试光路示意图;(b)镀金星形标准靶样品的 SEM;(c)标准靶中心内环 SEM 放大图;(d)波带片固定在测试光路支架的光学显微镜图;(e)(f)波带片对星形标准靶样品的聚焦成像图

Fig. 7 Imaging testing of X-ray zone plates. (a) Schematic diagram of test optical path; (b) SEM of gold plated star type standard target samples; (c) standard target center inner ring SEM enlarged view; (d) an optical microscope image of a zone plate fixed to a test optical path bracket; (e)(f) focused imaging of a star type standard target sample using a zone plate

4 结 论

提出一种大尺寸 X 射线波带片的设计制备方法并完成成像测试。首先研究了原子层沉积法生长 Al_2O_3 和 HfO_2 薄膜的特性。结果表明,薄膜的均匀性良好,在 $\pm 1\%$ 以下。然后在直径为 $72 \mu\text{m}$ 的金丝表面交替沉积了 $10.11 \mu\text{m}$ 的 $\text{Al}_2\text{O}_3/\text{HfO}_2$ 多层膜,并采用陪片监测机制实现了对每个环带宽度的精确控制,环带宽度的误差不超过 2 nm,最外环宽度达到 25 nm。接着利用 FIB 技术进行切片和抛光,最终获得了高宽比为 43:1 的 X 射线波带片。在上海光源(BL08U1A)线站上的成像测试结果表明,该波带片实现了聚焦成像功能,验证了原子层沉积和 FIB 切片法制备大尺寸 X 射线波带片的可行性和巨大潜力。

参 考 文 献

- [1] Smith H I. 100 years of x rays: impact on micro- and nanofabrication[J]. Journal of Vacuum Science & Technology B: Microelectronics and Nanometer Structures, 1995, 13(6): 2323-2328.
- [2] Buonassisi T, Istratov A A, Heuer M, et al. Synchrotron-based investigations of the nature and impact of iron contamination in multicrystalline silicon solar cells[J]. Journal of Applied Physics, 2005, 97(7): 074901.
- [3] Kirz J, Jacobsen C, Howells M. Soft X-ray microscopes and their biological applications[J]. Quarterly Reviews of Biophysics, 1995, 28(1): 33-130.
- [4] 谢红兰, 邓彪, 杜国浩, 等. 上海光源 X 射线成像及其在材料科学上的应用研究进展[J]. 失效分析与预防, 2021, 16(1): 46-59, 69.
- [5] Xie H L, Deng B, Du G H, et al. Development of X-ray imaging methodology and its applications on material science at Shanghai synchrotron radiation facility[J]. Failure Analysis and Prevention, 2021, 16(1): 46-59, 69.
- [5] 孙天希. 毛细管 X 射线透镜技术及其应用[J]. 光学学报, 2022,

- 42(11): 1134002.
Sun T X. Capillary X-ray lens technology and its applications[J]. *Acta Optica Sinica*, 2022, 42(11): 1134002.
- [6] 李浩川, 黄秋实, 朱京涛, 等. 多层膜劳厄透镜对 8 keV X 射线的聚焦性能模拟研究[J]. *光学学报*, 2011, 31(8): 0834001.
Li H C, Huang Q S, Zhu J T, et al. Simulation on focusing performance of X-ray multilayer Laue lens for 8 keV X-ray[J]. *Acta Optica Sinica*, 2011, 31(8): 0834001.
- [7] Yan H F, Conley R, Bouet N, et al. Hard X-ray nanofocusing by multilayer Laue lenses[J]. *Journal of Physics D: Applied Physics*, 2014, 47(26): 263001.
- [8] Zhu J T, Tu Y C, Li H C, et al. X-ray nanometer focusing at the SSRF based on a multilayer Laue lens[J]. *Chinese Physics C*, 2015, 39(12): 128001.
- [9] Ocola L E, Maser J, Vogt S, et al. Tapered tilted linear zone plates for focusing hard X-rays[J]. *Proceedings of SPIE*, 2004, 5539: 165-173.
- [10] Keskinbora K, Robisch A L, Mayer M, et al. Multilayer Fresnel zone plates for high energy radiation resolve 21 nm features at 1.2 keV[J]. *Optics Express*, 2014, 22(15): 18440-18453.
- [11] 吴鹿杰, 文庆涛, 高雅增, 等. 基于原子层沉积技术的高精度多层膜 X 射线菲涅耳波带片的制备研究[J]. *光子学报*, 2021, 50(1): 0123001.
Wu L J, Wen Q T, Gao Y Z, et al. Investigation on the preparation of high precision multilayer X-ray Fresnel zone plates based on atomic layer deposition technology[J]. *Acta Photonica Sinica*, 2021, 50(1): 0123001.
- [12] 高雅增, 吴鹿杰, 卢维尔, 等. 基于严格耦合波理论的硬 X 射线菲涅耳波带片设计[J]. *光学学报*, 2021, 41(11): 1111002.
Gao Y Z, Wu L J, Lu W E, et al. Design of hard X-ray Fresnel zone plates based on rigorous coupled wave theory[J]. *Acta Optica Sinica*, 2021, 41(11): 1111002.
- [13] Maser J. Evaluation of the efficiency of zone plates with high aspect ratios by application of coupled wave theory[M]// Michette A G, Morrison G R, Buckley C J. *X-ray microscopy III*. Springer series in optical sciences. Heidelberg: Springer, 1992, 67: 104-106.
- [14] Rehbein S, Heim S, Guttman P, et al. Ultrahigh-resolution soft-x-ray microscopy with zone plates in high orders of diffraction[J]. *Physical Review Letters*, 2009, 103(11): 110801.
- [15] 傅绍军, 洪义麟, 陶晓明, 等. 软 X 射线聚焦波带片制备工艺的研究[J]. *光学学报*, 1995, 15(8): 1148-1150.
Fu S J, Hong Y L, Tao X M, et al. Fabrication of soft X-ray condenser zone plates[J]. *Acta Optica Sinica*, 1995, 15(8): 1148-1150.
- [16] 李海亮, 史丽娜, 牛洁斌, 等. 大高宽比硬 X 射线波带片制作及聚焦测试[J]. *光学精密工程*, 2017, 25(11): 2803-2809.
Li H L, Shi L N, Niu J B, et al. Fabrication and focusing test of hard X-ray zone plates with high aspect ratio[J]. *Optics and Precision Engineering*, 2017, 25(11): 2803-2809.
- [17] 王德强, 曹磊峰, 谢常青, 等. 电子束和 X 射线光刻制作高分辨率微波带片[J]. *半导体学报*, 2006, 27(6): 1147-1150.
Wang D Q, Cao L F, Xie C Q, et al. Fabrication of micro zone plates by E-beam and X-ray lithography[J]. *Chinese Journal of Semiconductors*, 2006, 27(6): 1147-1150.
- [18] 陈宜方. X 射线衍射光学部件的制备及其光学性能表征[J]. *光学精密工程*, 2017, 25(11): 2779-2795.
Chen Y F. Fabrication of diffractive X-ray optics and their performance characterization[J]. *Optics and Precision Engineering*, 2017, 25(11): 2779-2795.
- [19] 陈宜方. 电子束光刻研制高分辨 X 射线波带片透镜最新进展[J]. *光学学报*, 2022, 42(11): 1134005.
Chen Y F. Recent progress in nanofabrication of high resolution X-ray zone plate lenses by electron beam lithography[J]. *Acta Optica Sinica*, 2022, 42(11): 1134005.
- [20] Chao W L, Kim J, Rekawa S, et al. Demonstration of 12 nm resolution Fresnel zone plate lens based soft X-ray microscopy[J]. *Optics Express*, 2009, 17(20): 17669-17677.
- [21] Moldovan N, Divan R, Zeng H J, et al. Atomic layer deposition frequency-multiplied Fresnel zone plates for hard X-rays focusing[J]. *Journal of Vacuum Science & Technology A: Vacuum, Surfaces, and Films*, 2018, 36(1): 01A124.
- [22] Tamura S, Yasumoto M, Mihara T, et al. Multilayer Fresnel zone plate for high-energy X-ray by DC sputtering deposition[J]. *Vacuum*, 2002, 66(3/4): 495-499.
- [23] Düvel A, Rudolph D, Schmahl G. Fabrication of thick zone plates for multi-kilovolt X-rays[C]. *AIP Conference Proceedings*, 2000, 507(1): 607-614.
- [24] Takano H, Sumida K, Hiroto H, et al. Hard X-ray multilayer zone plate with 25-nm outermost zone width[J]. *Journal of Physics: Conference Series*, 2017, 849: 012052.
- [25] Tamura S, Yasumoto M, Kamijo N, et al. Development of a multilayer Fresnel zone plate for high-energy synchrotron radiation X-rays by DC sputtering deposition[J]. *Journal of Synchrotron Radiation*, 2002, 9(3): 154-159.
- [26] Eberl C, Döring F, Liese T, et al. Fabrication of laser deposited high-quality multilayer zone plates for hard X-ray nanofocusing[J]. *Applied Surface Science*, 2014, 307: 638-644.
- [27] Sanli U T, Jiao C G, Baluksian M, et al. 3D nanofabrication of high-resolution multilayer Fresnel zone plates[J]. *Advanced Science*, 2018, 5(9): 1800346.
- [28] Mayer M, Keskinbora K, Grévent C, et al. Efficient focusing of 8 keV X-rays with multilayer Fresnel zone plates fabricated by atomic layer deposition and focused ion beam milling[J]. *Journal of Synchrotron Radiation*, 2013, 20(3): 433-440.
- [29] Keskinbora K, Robisch A L, Mayer M, et al. Recent advances in use of atomic layer deposition and focused ion beams for fabrication of Fresnel zone plates for hard x-rays[J]. *Proceedings of SPIE*, 2013, 8851: 885119.
- [30] Kamijo N, Suzuki Y, Takano H, et al. Microbeam of 100 keV x ray with a sputtered-sliced Fresnel zone plate[J]. *Review of Scientific Instruments*, 2003, 74(12): 5101-5104.
- [31] Pommert D A, Moharam M G, Grann E B. Limits of scalar diffraction theory for diffractive phase elements[J]. *Journal of the Optical Society of America A*, 1994, 11(6): 1827-1834.
- [32] Zhang L J, Xu Z J, Zhang X Z, et al. Latest advances in soft X-ray spectromicroscopy at SSRF[J]. *Nuclear Science and Techniques*, 2015, 26(4): 3-13.

Preparation of X-Ray Fresnel Zone Plate by Atomic Layer Deposition and Focused Ion Beam Slicing

Tan Mingsheng^{1,3}, Ming Shuaiqiang¹, Wu Yufei^{1,3}, Lu Weier^{1,3*}, Li Yanli^{2**},
Kong Xiangdong^{2,3***}, Liu Haigang⁴, Xia Yang^{1,3}, Han Li^{2,3}

¹*Institute of Microelectronics, Chinese Academy of Sciences, Beijing 100029, China;*

²*Institute of Electrical Engineering, Chinese Academy of Sciences, Beijing 100190, China;*

³*University of Chinese Academy of Sciences, Beijing 100049, China;*

⁴*Shanghai Synchrotron Radiation Facility, Shanghai Advanced Research Institute, Chinese Academy of Sciences, Shanghai 201800, China*

Abstract

Objective Fresnel zone plate (FZP) is one of the most important components in X-ray microscopic imaging systems, which can realize high-efficiency and high-resolution three-dimensional (3D) nondestructive imaging by diffraction principle. It is considered as one of the most potential devices to improve the quality of X-ray microscopic imaging and has been widely used in metal flaw detection, cell imaging, material testing, and other fields. High X-ray microscopic imaging quality means the high imaging resolution and diffraction efficiency which expects X-ray FZP with a large aspect ratio, that is, small outermost zone width and large thickness. The conventional fabrication technique of X-ray FZP is based on the most accurate lithography technique, namely e-beam lithography (EBL). However, the combination of large FZP thickness and small outermost zone width is usually out of the limits of EBL. Multilayer FZP (ML-FZP) is a promising solution to fabricate high-aspect-ratio FZP due to the unique sputter-sliced technique. Especially, the technique of atomic layer deposition (ALD) and focused ion beam (FIB) has emerged as an attractive combination to fabricate ML-FZP. Due to self-limiting surface reaction, ALD can realize atomic-scale precision in layer thickness and excellent conformality on the cylindrical substrate and is capable of coating many substrates simultaneously. The slicing and polishing processes both can be completed with FIB equipment. In order to meet the demand of a large aspect ratio of the zone plate for X-ray application, in this paper, multilayer films with high precision control of thickness were grown on a smooth surface of metal wire by ALD, and then ML-FZP with a large aspect ratio was obtained by FIB slicing.

Methods First, The X-ray ML-FZP with $\text{Al}_2\text{O}_3/\text{HfO}_2$ as bright and dark ring materials was designed by the complex amplitude superposition method. Then, $\text{Al}_2\text{O}_3/\text{HfO}_2$ multilayer films were alternately deposited on the surface of gold wire with a diameter of 72 μm by ALD. The layers were grown in a double-cavity rapid ALD equipment at the substrate temperature of 150 $^\circ\text{C}$ with a chamber pressure of 0.2 Torr. Al_2O_3 and HfO_2 depositions were carried out by taking trimethyl aluminum (TMA) and tetrakis (dimethylamino) hafnium (TDMAH) as metal sources and H_2O as the oxygen source. TDMAH was heated at 75 $^\circ\text{C}$ during the deposition process. The deposition processes for $\text{Al}_2\text{O}_3(\text{HfO}_2)$ were performed with TMA and TDMAH pulses of 0.02 and 0.08 s, N_2 purge of 10 and 15 s, H_2O pulse of 0.015 s, and another N_2 purge of 10 s, respectively. During the whole process, the deposition was stopped many times to clean the chamber or check the film growth rate due to the extremely long growth time. Some silicon slices were put in the chamber around the gold wires during the deposition. By monitoring the growth of multilayer films on silicon slices, the film growth rate was corrected in time. After the deposition of all the $\text{Al}_2\text{O}_3/\text{HfO}_2$ layers, the surface of the multilayer fiber was coated by a layer of Cr which was used to protect the multilayer structure from damage in subsequent processes. The large focused Ga^+ beam was used for slicing, and the beam current was 65 nA. Then the small Ga^+ beam of 5 nA was used for polishing the two surfaces of the zone plate. Finally, the X-ray FZP with a specific thickness was obtained. The prepared ML-FZP was applied to the soft X-ray imaging line station of Shanghai Synchrotron Radiation Facility (BL08U1A), and the focusing imaging function was realized under the X-ray of 1.2 keV. The resolving capability of the ML-FZP was analyzed by a gold-plated star test sample.

Results and Discussions The uniformity of the Al_2O_3 and HfO_2 films deposited by ALD was below $\pm 1\%$ (Fig. 3). The multilayer film consisted of 356 layers with an extremely large zone thickness of 10.11 μm and outermost zone width of 25 nm, and for each layer, the film thickness control precision was below 2 nm (Fig. 4). Through slicing and polishing of FIB, the ML-FZP with a height 1.08 μm and an aspect ratio of 43 : 1 was obtained. As shown in Fig. 7(f), the imaging resolution was about 800 nm. Although the ML-FZP showed imaging capacity, the properties could be further improved by optimizing the structure of ML-FZP. As the total zone thickness increased, special attention was required to minimize

the imperfection of ML-FZP. In the next step, we will optimize the combination of multilayer films and use films with positive and negative stresses alternately to reduce or eliminate the adverse effect caused by stress, so as to improve the imaging resolution.

Conclusions In this paper, the design and fabrication method of large-size X-ray ML-FZP and the imaging test were completed. First, the characteristics of Al_2O_3 and HfO_2 films grown by ALD were studied. The results showed that the uniformity of the films was below $\pm 1\%$. $\text{Al}_2\text{O}_3/\text{HfO}_2$ multilayers with a thickness of $10.11\ \mu\text{m}$ were alternately deposited on the surface of gold wire with a diameter of $72\ \mu\text{m}$, and a foil monitoring mechanism was proposed to achieve accurate control of each band width so that the error of the band width will not exceed $2\ \text{nm}$, and the outermost ring width will reach $25\ \text{nm}$. Then FIB technology was used for slicing and polishing, and an X-ray ML-FZP with an aspect ratio of $43 : 1$ was finally obtained. The imaging test of the zone plate was carried out at the BL08U1A line station, and the focusing imaging resolution of about $800\ \text{nm}$ was achieved. The feasibility and great potential of preparing large-size X-ray zone plates by ALD and FIB slicing were successfully verified. Future priorities include searching for the appropriate way of film stress release to avoid cracks and the precise thickness control of all multilayer films for realizing imaging performance.

Key words X-ray Fresnel zone plate; atomic layer deposition; focused ion beam; large aspect ratio; multilayer film